Journal of Molecular Structure 1352 (2026) 144555

Contents lists available at ScienceDirect

Journal of Molecular Structure

journal homepage: www.elsevier.com/locate/molstr

# Synthesis, structural elucidation, Hirshfeld surface, DFT, pharmacophore, and in silico studies of a piperonal derivative: A study based on experimental and theoretical methods

Darshan D. [a,b], Santhosh C. [c], Ravi Singh K. [c], Chethan B. S. [d], Lohith T. N. [e], Sadashiva M. P. [c], Sunil K. [a,*], Hemalatha P. [a,*]

[a] Department of Chemistry, Sri Siddhartha Institute of Technology, SSAHE, Tumkur, Karnataka 572105, India
[b] Department of Chemistry, Government First Grade College, Madhugiri, Karnataka 572132, India
[c] Department of Studies in Chemistry, University of Mysore, Manasagangotri, Mysuru, Karnataka 570 006, India
[d] Department of Physics, Sri Siddhartha Institute of Technology, SSAHE, Tumkur, Karnataka 572105, India
[e] Department of Physics, The National Institute of Engineering, Mysuru, Karnataka 570 008, India

ARTICLE INFO

*Keywords:*
Piperonal derivative
X-ray crystallography
Hirshfeld surface
Density functional theory
Molecular docking
Non-covalent interactions

ABSTRACT

A novel piperonal derivative, *2-((benzo[d][1,3]dioxol-5-ylmethyl)amino)-2-thioxo-N-(p-tolyl)acetamide* (**3a**) was synthesized and extensively characterized using advanced spectroscopic techniques (FT-IR, NMR), single-crystal X-ray diffraction, Hirshfeld surface analysis, Density Functional Theory (DFT) calculations, and molecular docking studies. Structural analyses confirmed the presence of the characteristic amide linkage and elucidated distinct supramolecular architectures stabilized predominantly by hydrogen bond (N—H…O) and C—H…π stacking interactions. Hirshfeld surface mappings quantified intermolecular interactions, revealing significant contributions from aromatic stacking contacts. The DFT calculations were performed using B3LYP functional and 6–311++*G* (d,p) basis set. Quantum chemical analyses highlighted extensive electron de-localization across the molecule, with subtle differences in electronic descriptors suggesting slightly higher reactivity. The energy gap of the compound is found to be 4.000 eV. The docking analysis of 3a with the protein 5F19, which is implicated in dual-action therapeutic targeting inflammation and tumorigenesis through soluble epoxide hydrolase inhibition.

## 1. Introduction

Although there have been advancements in the development of novel drugs and vaccines, cancer continues to be a leading cause of mortality in both industrialized and developing nations. In 2012 alone, global cancer cases reached approximately 14.1 million, resulting in 8.2 million deaths. Southeast Asia reported a significant number of life-threatening cancer cases, including breast, gastric, colorectal, and hepatocellular carcinomas [1–4]. Cancer originates from the gradual accumulation of genetic mutations that transform normal cells into malignant ones. These alterations at the cellular and molecular levels introduce complexities that make effective treatment difficult [5–8]. Traditional approaches such as chemotherapy, radiotherapy, and surgery remain the mainstays of cancer management. However, patients diagnosed at advanced stages or with solid tumors often face poor outcomes due to metastasis and various genetic or epigenetic abnormalities, highlighting the limited success of existing therapies. Therefore, there is a pressing need for the development of more effective drugs for both early and late-stage cancers [9–12].

Naturally occurring heterocyclic compounds have made a substantial contribution to medicinal chemistry, particularly in oncology. Amino-substituted heterocycles—such as aplysinopsine and clathridine—are among the most extensively studied for their potential against cancer, inflammation, and neurological disorders like Alzheimer's disease and Down syndrome [13–16]. Leucettamine B, a compound derived from Leucetta microraphis that includes an amino-imidazole ring and a piperonal moiety, also belongs to this group. However, its anti-cancer potential has yet to be fully explored. In this study, we evaluated leucettamine B and its derivatives for their effects on various cancer cell lines. Beyond these compounds, numerous other heterocycles have played vital roles in drug discovery for decades [17–19]. Notable examples include thiazolidinone,

* Corresponding authors.
*E-mail addresses:* sunilk999@gmail.com (S. K.), hemalathap@ssit.edu.in (H. P.).

https://doi.org/10.1016/j.molstruc.2025.144555
Received 14 September 2025; Received in revised form 23 October 2025; Accepted 26 October 2025
Available online 27 October 2025
0022-2860/© 2025 Elsevier B.V. All rights are reserved, including those for text and data mining, AI training, and similar technologies.

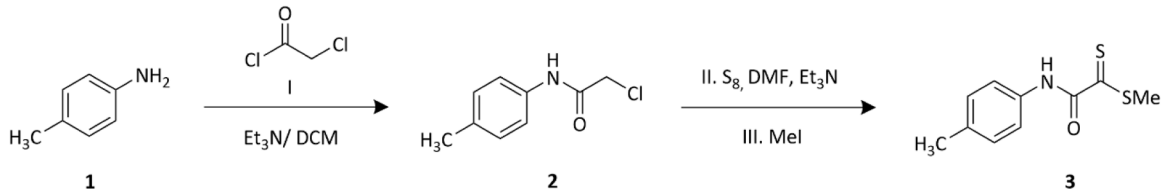


**Scheme 1.** Synthetic pathway of Methyl-2-oxo-2-(*p*-tolylamino)ethanedithioate **3. Reaction conditions: 1** (1.07 g, 1 equiv.), **I.** (1.11 g, 1 equiv.), **$Et_3N$** (2.02 g, 2 equiv.), DCM (10 mL), 0 °C-RT. **II. $S_8$** (0.64 g, 0.25 equiv.), **$Et_3N$** (2.02 g, 2 equiv.), DMF (20 mL), 0 °C-RT, 7–8 h, **III.** MeI (1.54 g, 1 equiv.), 0 °C-RT, 0.5 h.

thioxothiazolidin-4-one, and hydantoin derivatives. Of particular interest is the thiazolidin-2,4-dione (TZD) framework, which has been widely employed in therapeutic development. For instance, ciglitazone, the first anti-hyperglycemic agent in this class, was introduced in the 1980s, paving the way for related drugs like englitazone and rosiglitazone [20–22].

The compound *2-((benzo[d][1,3]dioxol-5-ylmethyl)amino)-2-thioxo-N-(p-tolyl)acetamide* (**3a**) exhibits promising potential for both anticancer and anti-arthritic activity based on its structural and electronic features. The presence of a *benzo[d][1,3]dioxole* ring, commonly found in bioactive natural products, suggests possible anticancer properties through mechanisms such as DNA intercalation, reactive oxygen species (ROS) modulation, or tubulin inhibition. The thioxo group (*C═S*) is known to facilitate electrophilic interactions, making it capable of covalently interacting with biological targets, including cancer-associated enzymes and cysteine-rich protein sites. Additionally, the acetamide and p-tolyl functionalities contribute to hydrogen bonding and hydrophobic interactions, enhancing its binding affinity within biological targets. From an anti-arthritic perspective, the structure resembles known COX-2 inhibitors, and molecular electrostatic potential (MEP) analysis reveals electron-rich zones conducive to interactions with key COX-2 active site residues as seen in the aspirin-acetylated COX-2 (PDB: 5F19) [23]. The compound also contains antioxidant-functional groups, which may reduce oxidative stress and inflammation associated with arthritis. Together, these features support the hypothesis that this molecule could act as a dual-action therapeutic agent with both anticancer and anti-inflammatory properties, warranting further investigation through molecular docking, ADMET prediction, and biological assays.

## 2. Materials and methods

All chemicals utilized in this work were purchase from reputed suppliers, like Merck, TCI and Sigma Aldrich and were used as received without further purification. Reactions were conducted using magnetic stirrer at temperature ranging from 0 °C to room temperature. UV lamp (254 nm) visualization were employed to monitor all the reaction using thin-layer chromatography on 60-$F_{254}$ precoated silica gel plates (0.25 mm thickness). All workup procedures were carried out by using double deionized water and ethyl acetate. Starting material and final products were purified *via* column chromatography using ethyl acetate/ hexane as eluents. Nuclear magnetic resonance (NMR) spectra were measured on Bruker 400 MHz instrument. $^{13}C$ NMR spectra were collected at 101 MHz using DMSO-$D_6$ and $CDCl_3$ as a solvent. Chemical shift values (δ) were reported in parts per million (ppm) relative to tetramethylsilane (TMS), as an internal standard with residual solvent peaks at 2.50 ppm (DMSO), 7.26 ppm ($CDCl_3$) for $^1H$ and 39.50 ppm (DMSO), 77.16 ppm for $^{13}C$. Coupling constant (J) values were given in Hertz (Hz). Bruker spectrophotometer was utilized to record the Fourier transform infrared spectra (FTIR). High-resolution mass spectrometry (HRMS) data were recorded using a Xevo TQD Quadrupole instrument. Sonar melting point apparatus was used to measure the melting points of intermediate and final product and are uncorrected.

### 2.1. Synthesis

#### 2.1.1. Synthesis of methyl-2-oxo-2-(p-tolylamino)ethanedithioate (3)

The synthesis of required intermediate methyl-2-oxo-2-(*p*-tolylamino)ethanedithioate (**3**), was accomplished through multi-step sequence as depicted in Scheme 1. The process begins with the treatment of *p-toluidine* **1** (1.07 g, 1 equiv.) in dichloromethane (DCM, 10 mL), at 0 °C with triethylamine (2.02 g, 2 equiv.), followed by dropwise addition of *chloroacetyl chloride* **I** (1.11 g, 1 equiv.), resulting in the formation of 2-chloro-N-(*p*-tolyl)acetamide **2.** Subsequently, compound **2** was converted to methyl-2-oxo-2-(p-tolylamino)ethanedithioate **3** *via* reaction with elemental sulfur **II** (0.64 g, 0.25 equiv.) in DMF (20 mL) at 0 °C, followed by the addition of triethylamine (2.02 g, 2 equiv.). The reaction mixture was stirred at room temperature for 7–8 h and then concentrated under reduced pressure. The resulting mixture was then treated with *methyl iodide* **III** to form the required substrate **3** in excellent yield (92 %). The spectroscopic characterizations such as $^1H$ NMR and $^{13}C$ NMR of the compound were performed and the spectra are provided in the Fig. S1 and S2 respectively.

#### 2.1.2. Synthesis of 2-((benzo[d][1,3]dioxol-5-ylmethyl)amino)-2-thioxo-N-(p-tolyl)acetamide (3a)

Piperonylamine, or 1,3-benzodioxole-5-methylamine, is a bioactive compound structurally related to several important pharmacological molecules. It is derived from piperonal an aldehyde originate in vital oils of plants like black pepper and kava. Due to its extensive range of

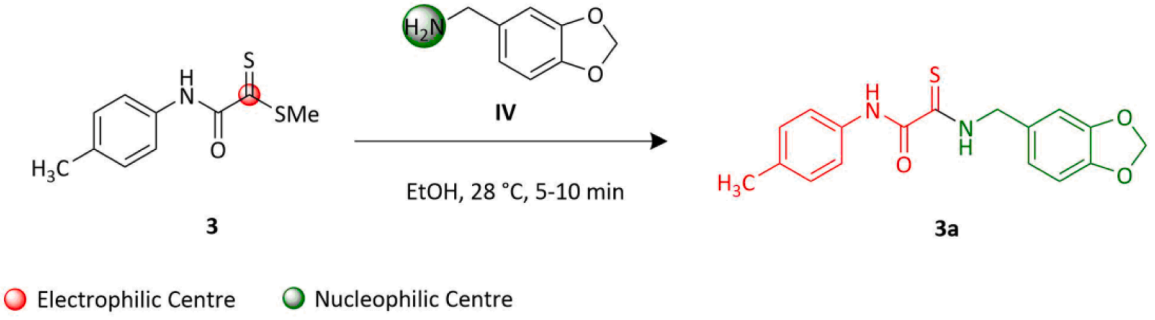


**Scheme 2.** Synthetic pathway of 2-((benzo[d][1,3]dioxol-5-ylmethyl)amino)-2-thioxo-N-(p-tolyl)acetamide (**3a**). **Reaction conditions: 3** (0.225 g, 1 equiv.), **IV** (0.151 g, 1 equiv.), EtOH (15 mL), 28 °C, 5–10 min.

**Table 1**
Crystal and structure refinement details of the compound **3a**.

| Parameters | Values |
|---|---|
| CCDC NO. | 2475,700 |
| Empirical formula | $C_{17}H_{16}N_2O_3S$ |
| Formula weight | 328.38 |
| Temperature | 300 K |
| Wavelength | 0.71073 Å |
| Reflns. for cell determination | 9575 |
| θ range for above | 2.27° to 25.42° |
| Crystal system | Monoclinic |
| Space group | $P2_1/n$ |
| Cell dimensions | $a = 4.8391(5)$ Å<br>$b = 26.258(3)$ Å<br>$c = 12.3960(12)$ Å<br>$\alpha = 90°$<br>$\beta = 95.987(3)°$<br>$\gamma = 90°$ |
| Volume | 1566.5(3) $Å^3$ |
| Z | 4 |
| Density(calculated) | 1.392 Mg $m^{-3}$ |
| Absorption coefficient | 0.223 $mm^{-1}$ |
| $F_{000}$ | 688 |
| Crystal size | 0.110 × 0.191 × 0.206 mm |
| θ range for data collection | 1.83° to 28.27° |
| Index ranges | $-6 \le h \le 6$<br>$-34 \le k \le 34$<br>$-15 \le l \le 16$ |
| Reflections collected | 30,244 |
| Independent reflections | 3884 [$R_{int} = 0.054$] |
| Absorption correction | Multi-scan |
| Refinement method | full matrix least-squares on $F^2$ |
| Data / restraints / parameters | 3884 / 0 / 212 |
| Goodness-of-fit on $F^2$ | 1.019 |
| Final $R$ indices [$I > 2\sigma(I)$] | $R1 = 0.0491$, $wR2 = 0.1250$ |
| $R$ indices (all data) | $R1 = 0.0819$, $wR2 = 0.1494$ |
| Largest diff. peak and hole | 0.214; −0.246 e $Å^{-3}$ |

biological and pharmacological activities, piperonylamine and its derivatives have gathered significant attention. The compound readily undergoes condensation reactions, facilitating the formation of diverse functional derivatives with enhanced bioactivity. The present report details the synthesis of 2-((benzo[d][1,3]dioxol-5-ylmethyl)amino)-2-thioxo-N-(p-tolyl)acetamide via simple condensation reaction. Thus equimolar ratios of Methyl-2-oxo-2-(p-tolylamino)ethanedithioate **3** (0.225 g, 1 equiv.) and benzo[d][1,3]dioxol-5-ylmethanamine **IV** (0.151 g, 1 equiv.) were combined in 2 mL of EtOH and stirred for 5–10 min. The progress of the reaction was monitored by TLC. After completion, the solvent was evaporated under reduced pressure, and the resulting compound was extracted with ethyl acetate and water. The aqueous layer was extracted multiple time with ethyl acetate, and the combined organic layer was dried over $Na_2SO_4$ and concentrated under reduced pressure. The crude product was purified by column chromatography on silica gel using hexane/ethyl acetate (86:14) eluent, affording 2-((benzo[d][1,3]dioxol-5-ylmethyl)amino)-2-thioxo-N-(p-tolyl)acetamide **3a**, as shown in Scheme 2.

A fine single crystal of **3a** fit for XRD analysis was obtained by slow evaporation of an ethyl acetate solution (50 mg of compound **3a** dissolved in 6–8 mL) over 30–35 h at room temperature. The molecular structure of compound **3a** was subsequently confirmed through single-crystal X-ray diffraction analysis.

#### 2.1.3. Spectroscopic characterizations

**Methyl 2-oxo-2-(p-tolylamino)ethanedithioate (3):** Red solid; Yield 2.071 g (92 %); $^1$H NMR (400 MHz, DMSO): δ 10.35 (s, 1H, NH), 7.61 (d, $J$ = 7.7 Hz, 2H, Ar-H), 7.17 (d, $J$ = 8.3 Hz, 2H, Ar-H), 2.71 (s, 3H), 2.27 (s, 3H).$^{13}$C NMR (101 MHz, DMSO) δ 226.75, 160.75, 135.09, 133.84, 129.18, 120.51, 20.49, 19.25. HRMS (ESI): $m/z$[$M$ + H]$^+$calcd for $C_{10}H_{12}NOS_2$: 226.0360; found: 226.0364 (Fig. S1 and S2).

**2-((benzo [d] [1,3] dioxol-5-ylmethyl)amino)-2-thioxo-N-(p-tolyl)acetamide (3a):** Yellow solid; mp 122–124 °C Yield 0.288 g (88 %); $^1$H NMR (400 MHz, $CDCl_3$): δ 10.13 (s, 1H, NH), 9.74 (s, 1H, NH), 7.57 (d, $J$ = 8.5 Hz, 2H, Ar-H), 7.21 (d, $J$ = 8.0 Hz, 2H, Ar-H), 6.89 – 6.78 (m, 3H, Ar-H), 6.00 (s, 2H, Het-H), 4.78 (d, $J$ = 5.7 Hz, 2H, $CH_2$), 2.37 (s, 3H, $CH_3$).$^{13}$C NMR (101 MHz, $CDCl_3$): δ 186.2, 155.7, 148.2, 147.7, 135.2, 134.1, 129.7, 128.6, 122.0, 119.8, 108.9, 108.6, 101.3, 50.3, 21.0;(Fig. S3 and S4 in the supplementary file), IR: $\upsilon_{max}$($cm^{-1}$) 831, 931, 1099, 1261, 1441, 1532, 1592, 1668, 3237 (Fig. S5 in the supplementary file); HRMS (ESI) $m/z$: [$M$ + H]$^+$ calcd. for $C_{17}H_{17}N_2O_3S$ 329.0960; found 329.0977 (Fig. S6 in the supplementary file).

### 2.2. X-ray crystallography

A single crystal of $C_{17}H_{16}N_2O_3S$ (**3a**) dark yellow in color measuring 0.110 × 0.191 × 0.206 mm was selected using a polarizing microscope and was then placed on the goniometer to collect X-ray intensity data. Additionally, utilizing a Bruker APEX-II CCD instrument with an IμS Mo micro source (λ = 0.7107 Å) at ambient temperature, the single crystal X-ray structure of **3a** was successfully obtained. The Bruker Apex 2 software package was used to analyze the raw data frames and apply absorption adjustments. The intrinsic phasing method was used to solve the compound's structure, which was then improved using the SHELXL [24] program and extended using Fourier techniques. All non-hydrogen atoms were given anisotropic displacement parameters, and all hydrogen atoms were geometrically positioned using the riding model [25]. The full matrix least squares method was used to refine the non-hydrogen atoms anisotropically after the structure was solved and refined using 3884 distinct reflections out of 30,244 total reflections. The $R$ value convergence to a residual value of 0.0491 and a goodness of fit of 1.019. Geometrical parameters such as bond lengths, bond angles, and torsion angles were calculated using the PLATON software [26]. The ORTEP and packing diagrams were created using the MERCURY 4.2.0 program [27]. Crystal and structure refinement details of the compound **3a** are given in Table 1.

### 2.3. Hirshfeld surface analysis

Hirshfeld surface analysis quantifies and illustrates a molecular interactions of the compound **3a**. CrystalExplorer 17.5 software was used to generate relative 2-D fingerprint plots of Hirshfeld surfaces mapped across $d_{norm}$ (−0.4173 a.u. to 1.3625 a.u.), shape index (−1.0000 a.u. to 1.0000 a.u.), [28,29]. The Van der Waals radii, $d_e$ (outside) (range: 0.8669 a.u. to 2.6567 a.u.) and $d_i$ (inside) (range: 0.8675 a.u. to 2.5533 a.u.), represent the distances between the chosen molecule and the Hirshfeld surface. The crystallographic information file (CIF) was utilized to generate Hirshfeld surfaces and 2-D fingerprint maps for **3a**. Graphically plotting 3-D molecular Hirshfeld surfaces over the $d_{norm}$ identifies key areas for studying intermolecular interactions [30,31]. Hirshfeld surface analysis is used to investigate all potential structural contributions and better understanding of crystal packing in solid form. Additionally, the total interaction energy (sum of electronic, polarization, dispersive, and repulsive energies) was computed by simulating the molecular arrangement in the crystalline lattice using B3LYP/6–311+G (d,p) integrated in the CrystalExplorer 17.5 software [32].

### 2.4. DFT calculations

We can analyze the physical and chemical properties of a synthesized product based on its electron density [33]. To approximate electron wave functions, the electron density function from single crystal X-ray diffraction is used. The B3LYP hybrid functional and 6–311+G(d,p) [34] basis set were optimized for DFT analysis of these wave functions. Koopman's approximation was used to calculate the FMO analysis, energy gap, and global and local indices [35]. Further, the molecular electrostatic potential (MEP) map is an effective tool for finding electrophilic and nucleophilic regions. The MEP color-codes electrostatic

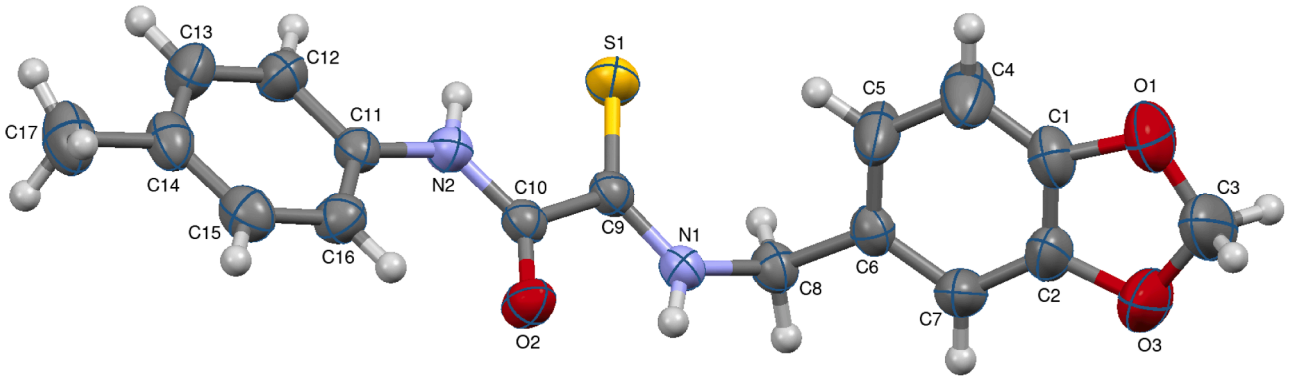


**Fig. 1.** ORTEP of the compound **3a**.

potential regions, ranging from red to dark blue (decrease in potential, blue > green > yellow > orange > red), to indicate extremely negative and positive places [36]. The molecular electrostatic potential map was used to identify the molecule's potential reactive spots. All computations were performed using Gaussian 09 [37], and the results were displayed using GaussView 6.0 [38].

### 2.5. Molecular docking analysis

Molecular docking analysis is used to determine a ligand's affinity for a specific protein. Molecular docking analysis may depict how a ligand interacts with a protein to decrease its activity in the biological system [39,40]. Literature review suggests that the produced molecule may have anti-cancer capabilities, as similar medicines have been shown to inhibit cancer. The new compound is docked against the 5F19 protein, a target for cancer and arthritis. The protein (PDB ID: 5F19) was retrieved from the RCSB-PDB database. Biovia Discovery Studio [41] was used to create the ligand pdb file for the compound studied. Auto-DockTools 1.5.6 [42] was used to generate pdbqt files for both the protein and its ligand. The molecule was docked against the protein PDB ID: 5F19, with grid dimensions of $X = 56$, $Y = 64$, and $Z = 60$. Additionally, the grid center is at $X = -1.353$, $Y = -1.396$, and $Z = 32.242$. Biovia Discovery Studio software was used to visualize ligand-protein interactions and docking conformations.

### 2.6. ADMET profiles

The drug-likeness of the novel compound was evaluated using the SwissADME and pkCSM online tools, which predict key pharmacokinetic parameters such as absorption, distribution, metabolism, and excretion (ADME) [42,43]. These tools also provide insights into lipophilicity and various physicochemical characteristics of the compound. The bioavailability radar generated by SwissADME visually summarizes crucial physicochemical properties—such as lipophilicity, molecular size, polarity, and flexibility—that influence oral bioavailability, enabling a quick assessment of the compound's potential as a viable drug candidate [44,45]. Additionally, toxicity and pharmacokinetic profiles were further predicted using the pkCSM tool.

## 3. Results and discussions

### 3.1. Synthesis

The structural validation of the synthesized compound **3a** was scrupulously established using various spectroscopic techniques, like FTIR spectroscopy, Nuclear magnetic resonance (NMR) spectroscopy and High-Resolution Mass Spectroscopy (HRMS). $^{1}$H NMR spectrum of compound **3a** was recorded in $CDCl_3$, on a 400 MHz Bruker spectrometer, displayed 16 distinct proton signals. Notably, two characteristic singlet peaks at 10.13 and 9.73 ppm correspond to the two non-equivalent amide and thioamide NH protons, which do not show coupling due to rapid exchange under the experimental conditions. The singlet at δ 5.99 ppm (2H) corresponds to the methylenedioxy (–O–$CH_2$–O–) group, which appears as a singlet due to the absence of neighboring protons indicating the successful condensation of amines with thioesters. The multiplet observed between δ 6.89 – 6.78 ppm corresponds to the aromatic protons of the benzo[d][1,3]dioxole ring, where overlapping of *ortho* and *meta* couplings produce a complex pattern. The *para*-tolyl group was evident from two doublet signals at 7.57 and 7.55 ppm with coupling constants of $J = 8.5$ and 8.0 Hz, respectively, indicating typical *ortho* coupling between adjacent aromatic protons within a para-substituted benzene ring. A singlet peak at 2.36 ppm (3H) represents the methyl group attached to the p-tolyl ring, with no coupling since it is magnetically isolated altogether attributes to the structural confirmation of the synthesized compound. The $^{13}$C NMR spectrum of compound **3a** exhibited fifteen distinct carbon resonances consistent with the proposed structure. The signal at δ 186.2 ppm corresponds to the thiocarbonyl carbon (*C*═*S*) of the thioamide group, appearing at a characteristic downfield position due to the strong deshielding effect of the sulfur atom. The resonance at δ 155.7 ppm is attributed to the amide carbon (*C*═*O*), confirming the presence of the thioamide framework. The signals at δ 148.2 and 147.7 ppm are consigned to the oxygen-bearing aromatic carbons of the benzo[d][1,3] dioxole ring, which are deshielded by the adjacent methylenedioxy group. The peaks at δ 135.2 and 134.1 ppm correspond to the quaternary aromatic carbons of the p-tolyl and benzo[d][1,3]dioxole moieties. The aromatic CH carbons resonate at δ 129.7, 128.6, 122.0, and 119.8 ppm, representing the protonated aromatic carbons of both aromatic rings. The signals at δ 108.9, 108.6, and 101.3 ppm are typical of the methylenedioxy-substituted aromatic system, with δ 101.3 ppm assigned to the –O–$CH_2$–O– carbon. The benzylic methylene carbon ($CH_2$–NH) appears at δ 50.3 ppm, consistent with a carbon adjacent to a nitrogen atom. Finally, the methyl carbon of the p-tolyl group resonates at δ 21.0 ppm, characteristic of an aromatic methyl substituent. The overall $^{13}$C chemical shift pattern supports the proposed structure. The FTIR spectrum supported the structural assignments, showing a broad absorption at 3236 $cm^{-1}$ corresponds to N—H stretching vibrations of amide and thioamide groups. The C—H stretching band at 2915 $cm^{-1}$, typically associated methylene ($CH_2$) group. A prominent absorption peak at 1668 $cm^{-1}$ indicated the presence of a carbonyl (*C*═*O*) group, while the corresponding thiocarbonyl (*C*═*S*) stretch appeared at 1099 $cm^{-1}$. The absorption band at 1532 $cm^{-1}$ was attributed to (*C*═*C*) stretching vibration. Additionally, strong absorptions at 1261 and 1099 $cm^{-1}$ corresponded to C–N and C–S bond stretching, respectively. The absorptions at 931, and 831 $cm^{-1}$ are characteristic of the methylenedioxy (-O-$CH_2$-O-) group vibrations, confirming the presence of the benzo[d][1,3]dioxole ring. High-resolution mass spectrum (HRMS) spectrum of compound ***3a*** shows a molecular ion peak at *m*/*z*329.0977,

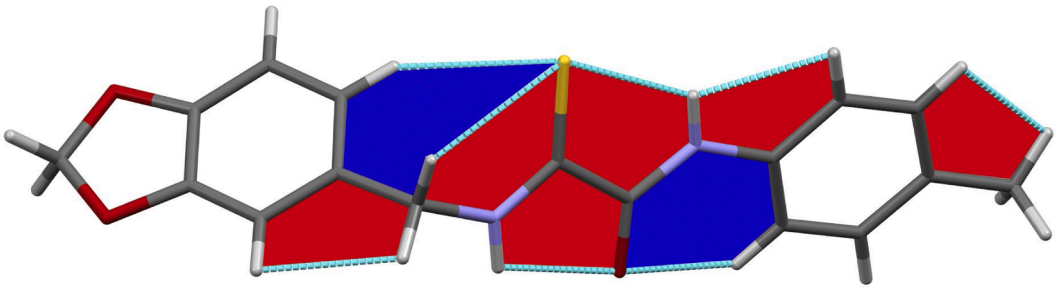

**Fig. 2.** Intramolecular interactions resulting in the formation of S(5) (red) and S(6) (blue) synthons.

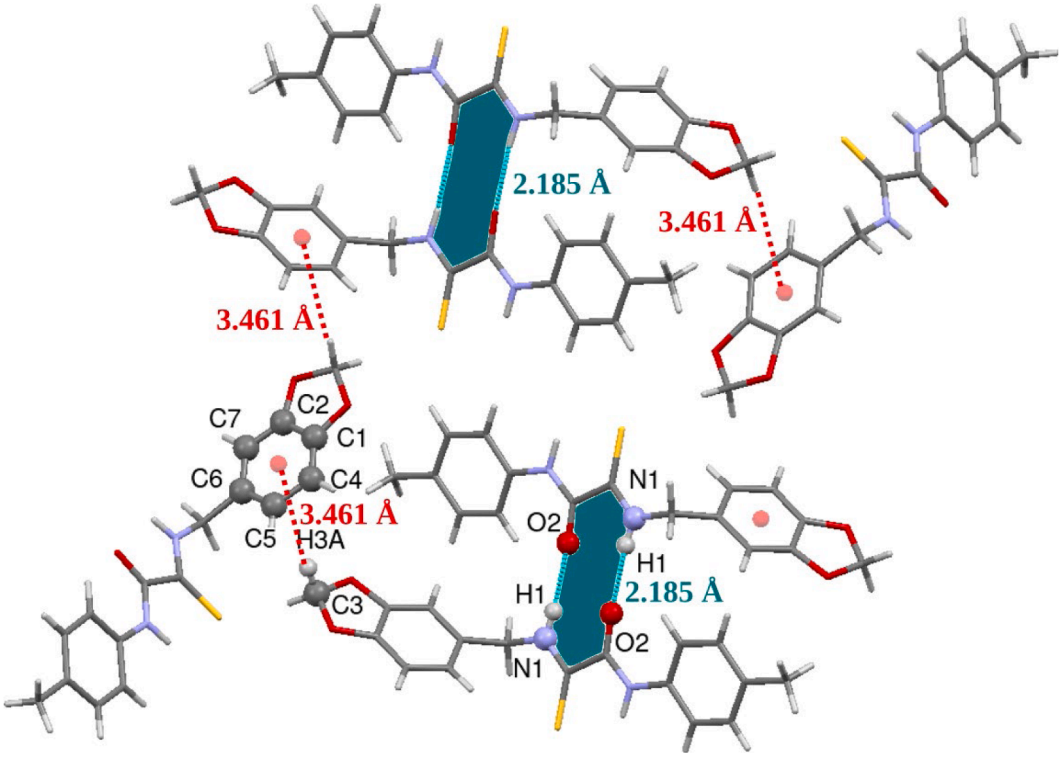


**Fig. 3.** Intermolecular interactions exhibited by the compound **3a**.

corresponding to the $[M + H]^+$ ion. This observed mass value is in excellent agreement with the calculated mass. All spectroscopic data including $^1$H and $^{13}$C NMR spectra, and FTIR are provided in the Fig. S3-S6 in the supporting information file.

### 3.2. X-ray crystallography

The 3D structure of the compound **3a** obtained by the single crystal X-ray diffraction study is shown in Fig. 1. The compound **3a** crystallizes in the monoclinic crystal system with $P2_1/n$ space group having unit cell parameters $a = 4.8391(5)$ Å, $b = 26.258(3)$ Å and $c = 12.3960(12)$ Å, $\beta = 95.987(3)^\circ$, $V = 1566.5(3)$ Å$^3$, $Z = 4$ (at 300 K). The geometrical parameters are listed in Table S1. The molecular geometry shows that the title compound consists of two rings namely; methylbenzene ring and Dihydro-1,3-benzodioxole. The formation of the compound due to the reaction between 5-methylbenzo[*d*][1,3]dioxole and 2-amino-2-thioxo-*N*-(*p*-tolyl)acetamide resulted in non planar nature with a dihedral angle of 80.28° Due to the lengthy nature of the 2-amino-2-thioxo-*N*-(*p*-tolyl)acetamide moiety and its linkage with the 5-methylbenzo[*d*][1,3]dioxole moiety through N—C bond resulted in the non planar arrangement.

The molecule exhibit anti-clinical conformation with respect to the torsional angle of the atoms (C6/C8/N1/C9) in the region of fusion between the two moieties. Due to the non planar nature of the compound various intra and intermolecular interactions were observed. The C—H..H/S/O (C7-H7…H8B, C12-H12…H1AA, C8-H8A…S1, C16-H16…O2) and interestingly N—H…O (N1-H1…O2) interactions resulted in the formation of S(5) and S(6) intramolecular synthons. The intramolecular interactions is shown in the Fig. 2. Further due to the N1-H1…O2 intermolecular interactions $R_2^2(10)$ supramolecular synthon is formed (Fig. 3). The NH atoms of the amino group attached to the *benzo[d][1,3]dioxol-5-yl* moiety acts as electron donor and Oxygen atom of the carbonyl group acts as electron acceptor in this interactions. The

**Table 2**
Intra and intermolecular interactions exhibited by the synthesized compound **3a**.

| Type | D-H…A | D-H (Å) | H…A (Å) | D…A (Å) | D-H…A (°) |
|---|---|---|---|---|---|
| Intra | N1-H1…O2 | 0.86 | 2.21 | 2.632(2) | 110 |
| Intra | N2-H1AA…S1 | 0.88 | 2.43 | 2.972(19) | 121 |
| Intra | C8-H8A…S1 | 0.97 | 2.74 | 3.151(2) | 106 |
| Intra | C16-H16…O2 | 0.93 | 2.36 | 2.936(3) | 120 |
| Inter | N1-H1…O2 | 0.86 | 2.18 | 2.938(2) | 146 |

**Table 3**
Various Cg…Cg interactions exhibited by the crystal structure.

| *CgI* | *CgJ* | Cg…Cg (Å) | Alpha (°) | Beta (°) | Gamma (°) | $CgI_{perp}$(Å) | $CgJ_{perp}$ (Å) | Slippage |
|---|---|---|---|---|---|---|---|---|
| Cg1 | Cg1 | 4.839(2) | 0.02(18) | 44.7 | 44.7 | 3.44(13) | −3.44(13) | 3.403 |
| Cg1 | Cg2 | 5.327(19) | 0.59(15) | 49.9 | 49.9 | 3.43(13) | −3.43(11) | 4.074 |
| Cg1 | Cg3 | 5.483(16) | 36.15(15) | 50.0 | 62.3 | 2.54(13) | 3.52(9) | |
| Cg1 | Cg4 | 5.012(18) | 0.31(14) | 46.8 | 46.8 | 3.42(13) | −3.43(9) | 3.651 |
| Cg2 | Cg2 | 4.839(17) | 0.03(13) | 45.0 | 45.0 | 3.42(11) | −3.42(11) | 3.420 |
| Cg2 | Cg4 | 4.899(16) | 0.29(11) | 45.8 | 45.6 | 3.42(11) | −3.41(9) | 3.510 |
| Cg4 | Cg1 | 4.956(18) | 0.31(14) | 46.2 | 46.0 | 3.44(9) | −3.43(13) | 3.577 |

**Cg1**: O1/C1/C2/O3/C3, **Cg2**: C1/C2/C7/C6/C5/C4,.
**Cg3**: C11/C12/C13/C14/C15/C16, **Cg4**: O1/C1/C4/C5/C6/C7C/C2/O3.

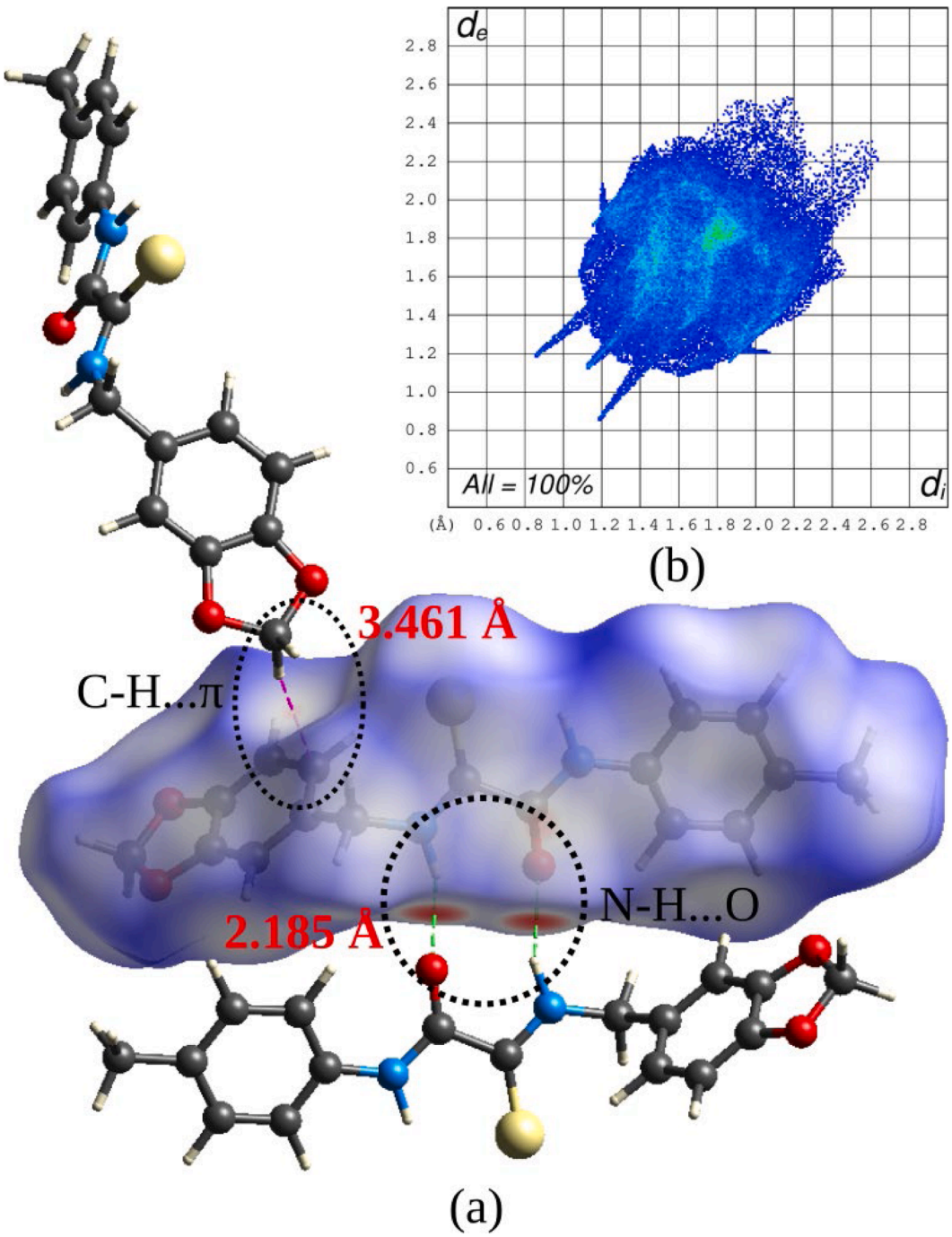


**Fig. 4.** (a) The $d_{norm}$ mapped Hirshfeld surface and (b) corresponding 2D finger print plot of the compound **3a**.

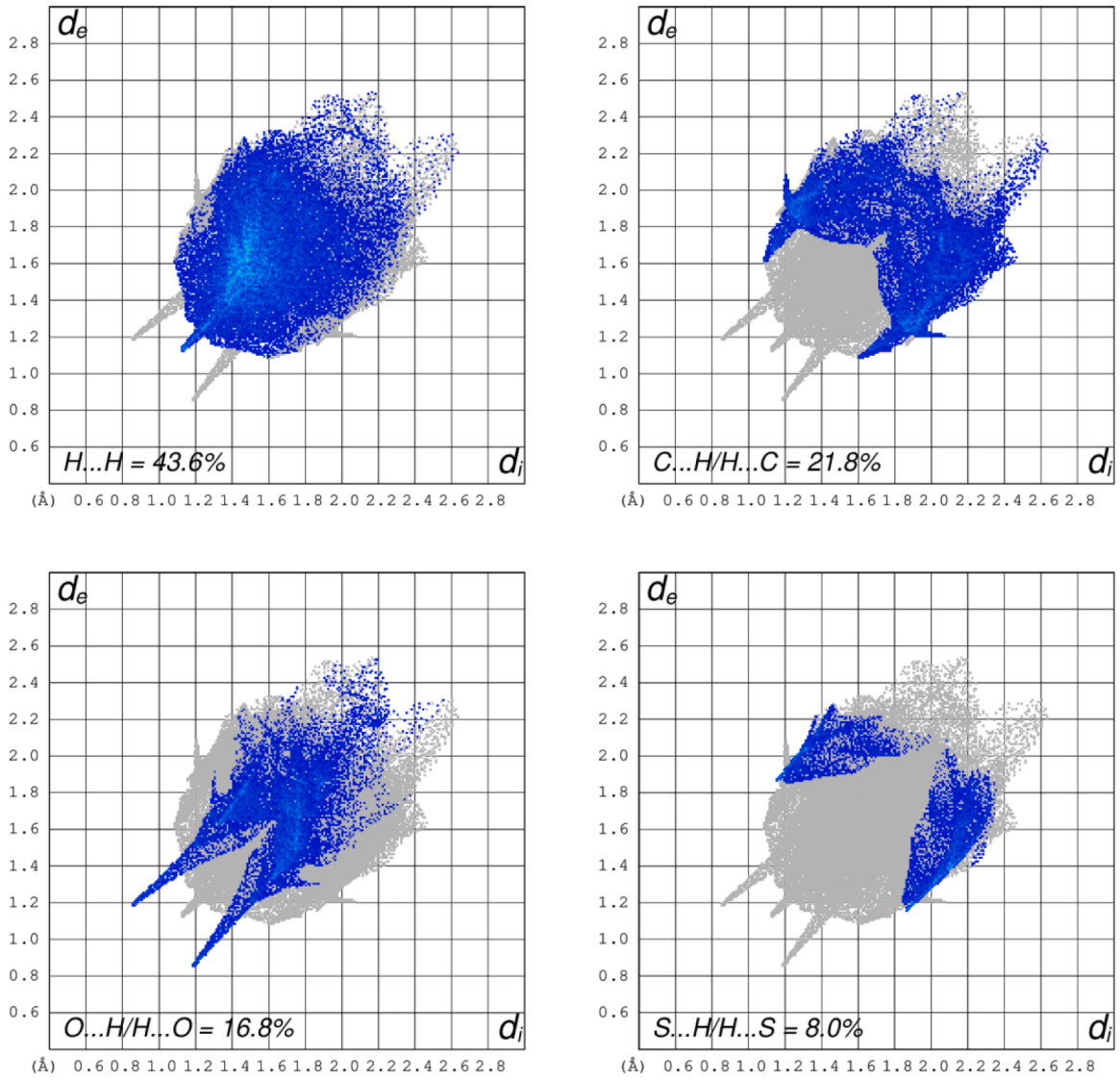


**Fig. 5.** 2D fingerprint plots of individual contacts present in the compound **3a**.

details of the intra and intermolecular interactions is provided in the Table 2.

Further, in addition to these interactions, the π…π/Cg…Cg interactions were observed to be significantly contributing towards the overall stability of the structure. The details of the Cg…Cg interactions exhibited by the structure is given in the Table 3. Further, a C—H…π interaction that is C17-H17A…Cg3 (C11/C12/C13/C14/C15/C16) was observed with C17…Cg3 distance of 3.649 (3) Å and with the angle of 133°

### 3.3. Hirshfeld surface analysis

Hirshfeld surfaces and fingerprint images are developed and displayed in Fig. 4 as an additional method for investigating intermolecular interactions; these surfaces were mapped using $d_{norm}$. The traditional N—H···O and C—H…π intermolecular hydrogen bonding interactions are clearly observed as bright and light-red spots, as seen in $d_{norm}$ surfaces (Fig. 8(a)). This demonstrates that it plays a substantial role in crystal packing since its distances are comparable to or noticeably less than the equivalent sum of Van der Waals radii. These red regions seen in Fig. 4 are validates the hydrogen bonds donor and acceptor atoms given in Table 2.

The Fig. 4(b) reveal the 2D fingerprint plots which quantifies the weak intermolecular interactions exhibited by the compound **3a**. The highest contributions to the Hirshfeld surfaces are from the H···H (43.6 %) interactions as indicated by the central spike in the 2D fingerprint plot. Further, C···H/H···C (21.8 %), O···H/ H···O (16.8 %), and S···H/ H···S (8.0 %) interactions are represented by blue spikes. The minor contacts (such as C···O, N···C, and S···H interactions) that contribute to the remaining ~10 % of the total Hirshfeld surface area [46]. Therefore, the whole fingerprint region and all other interactions, which are mixtures of $d_e$ and $d_i$ are displayed in Fig. 5. The $d_{norm}$-mapped Hirshfeld surface analysis displays intermolecular interactions as red patches, as seen in the crystallographic investigation. Shape index not only define their shape, but also show points of contact and provide information on molecular packing. The existence of C—H···π and π···π stacking interactions is shown by the flat green patches on the curvedness surface (Fig. 9(a)). Moreover, the shape index map reveals that the neighboring red and blue triangles in Fig. 6(a) indicate the C—H···π and π···π stacking weak interactions. The shape index on the Hirshfeld surface analysis can be used to examine interactions involving hydrogen donors (convex blue regions) and acceptors (concave red regions). The interaction of centroids in a crystal structure highlights contact faces and provides insight into molecular packing.

Crystal packing gaps suggest a close organization of molecules. A lower vacancy fraction indicates more crystal packing. The voids are

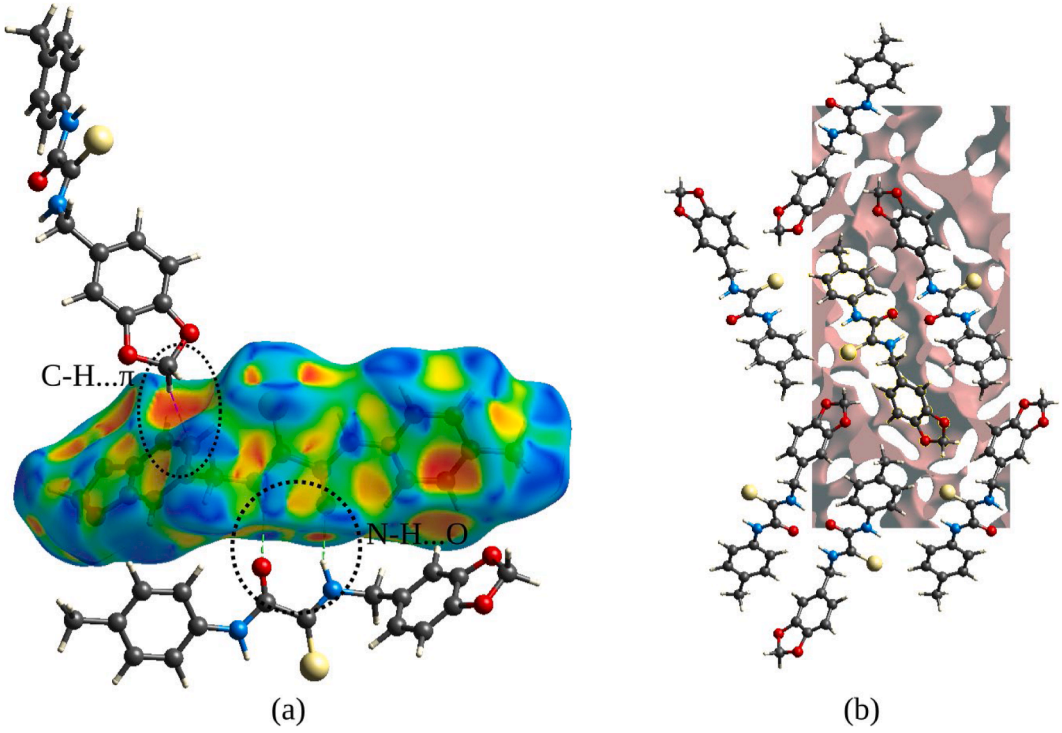


**Fig. 6.** (a) shape index property associated with Hirshfeld surface and (b) voids present in the unit cell of the compound **3a**.

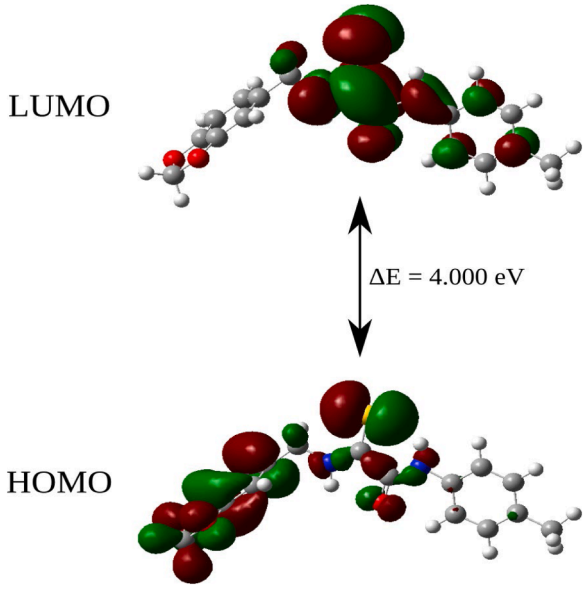


**Fig. 7.** HOMO-LUMO of the compound **3a**.

computed by adding the spherical electron densities at specified nuclear sites [47]. The crystal void calculation indicates a volume of 149.56 Å$^3$. The surface area was calculated to be 576.79 Å$^2$. Fig. 6(b) shows the voids in the crystal structure.

### 3.4. DFT calculations

#### 3.4.1. HOMO-LUMO analysis

The frontier molecular orbitals, i.e., HOMO and LUMO, are crucial in evaluating the electrical properties of quantum chemistry [48]. The HOMO orbital is highly localized on the piperonal ring and acetamide moiety. In contrast, the LUMO orbitals are found on the aromatic ring, with the electron-drawing carboxy group (Fig. 7). The energy gap is found to be 4.000 eV. A molecule with a limited or lowest orbital gap in terms of energy is thought to have lower kinetic stability and higher chemical reactivity. Chemical compounds with a larger energy difference between their highest (HOMO) and lowest molecular orbitals (LUMO) are said to have limited reactivity and the inability to be polarized. The ionization potential (I) is related to the energy of the highest occupied molecular orbital (HOMO) which acts as an electron donor whereas the LUMO act as electron-deficient and readily receive electrons. The electron affinity (A) is associated with the energy of the LUMO [49]. In short the ionization potential and electron affinity represented the nucleophilic and electrophilic character of the studied compound, respectively. The higher ionization potential ($I = 5.869$ eV) representing the significant nucleophilic character of studied compound. Compound **3a** was determined to be a reactive compound based on the observations made in Table 4.

**Table 4**
Global and local reactive parameters of the compound **3a**.

| Parameters | Values |
|---|---|
| $E_{HOMO}$ (eV) | −5.869 |
| $E_{LUMO}$ (eV) | −1.869 |
| Energy gap ($\Delta E_{LUMO\text{-}HOMO}$) (eV) | 4.000 |
| Ionization energy (I) (eV) | 5.869 |
| Electron affinity (A) (eV) | 1.869 |
| Electronegativity (χ) (eV) | 3.869 |
| Chemical potential (μ) (eV) | −3.869 |
| Global hardness (η) (eV) | 2.000 |
| Global softness (s) (eV$^{-1}$) | 0.500 |
| Electrophilicity index (ω) (eV) | 3.742 |

#### 3.4.2. Analysis of the conceptual DFT indices

The physiochemical attributes obtained from DFT are used to correlate the predicted energy with their quantum features. Quantum characteristics, including electronegativity (χ), electrophilicity (ω), hardness (η), and softness (S), are used to study the chemical behavior of molecules [50]. The hardness value indicates the atomic resistance to

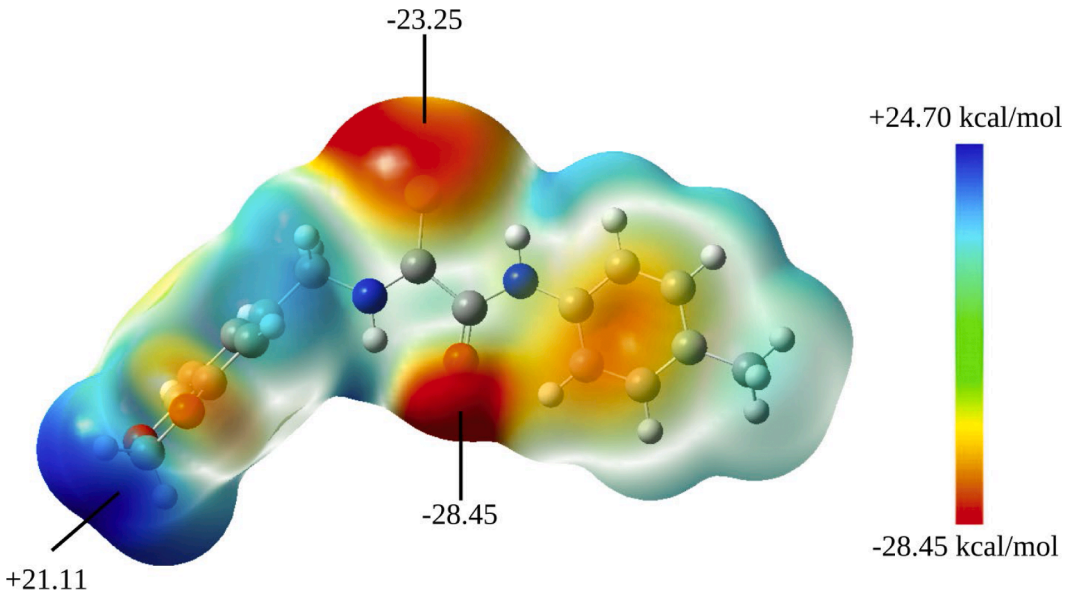


**Fig. 8.** MEP map of the compound **3a**.

charge transmission to neighboring atoms or molecules, whereas the softness parameter indicates the atom's electrophilicity. The research compound had a high softness value ($S$ = 0.500 eV), indicating that it was highly reactive. Electronegativity ($\chi$) describes a molecule's ability to attract electrons. The presence of electronegative oxygen and nitrogen atoms in the chemical structure resulted in significant electron attraction ($\chi$ = 3.869 eV).

### 3.4.3. *MEP analysis*

The Molecular Electrostatic Potential (MEP) map of 3a provides valuable insights into the charge distribution and reactive sites within the molecule (Fig. 8). The color-coded surface indicates regions of varying electrostatic potential, with red representing electron-rich (negative potential) areas and blue representing electron-deficient (positive potential) regions [51]. The most negative potential, measured at −28.45 kcal/mol, is observed near the thioxo group (C═S), identifying it as the most probable site for electrophilic attack due to the high electron density around the sulfur atom. A second significantly negative region (−23.25 kcal/mol) is located around the amide moiety, likely corresponding to the carbonyl oxygen or adjacent nitrogen, which also serves as a favorable site for interactions with electrophiles. In contrast, the most positive electrostatic potential (+21.11 kcal/mol) appears in the region surrounding the benzylic methylene group attached to the benzo[d][1,3]dioxole ring, suggesting a site susceptible to nucleophilic attack. The aromatic rings and remaining portions of the molecule exhibit intermediate potential (green to yellow areas), indicating relative electrostatic neutrality and potential involvement in non-covalent interactions such as π–π stacking or hydrophobic contacts. Overall, the MEP analysis highlights the thioxo sulfur and amide functionalities as key reactive centers, providing crucial guidance for understanding the molecule's potential binding behavior and biological activity, particularly in the context of drug–target interactions or molecular docking studies.

**Table 5**
ADMET profiles of the compound **3a**.

| Property | Model name | Predicted Value |
|---|---|---|
| Absorption | Water solubility | −4.17 |
| Absorption | Caco2 permeability | 1.31 |
| Absorption | Intestinal absorption (human) | 91.28 |
| Absorption | Skin Permeability | −3.29 |
| Absorption | P-glycoprotein substrate | Yes |
| Absorption | P-glycoprotein I inhibitor | Yes |
| Absorption | P-glycoprotein II inhibitor | No |
| Distribution | VDss (human) | −0.11 |
| Distribution | Fraction unbound (human) | 0.06 |
| Distribution | BBB permeability | 0.19 |
| Distribution | CNS permeability | −2.14 |
| Metabolism | CYP2D6 substrate | No |
| Metabolism | CYP3A4 substrate | Yes |
| Metabolism | CYP1A2 inhibitior | No |
| Metabolism | CYP2C19 inhibitior | Yes |
| Metabolism | CYP2C9 inhibitior | No |
| Metabolism | CYP2D6 inhibitior | No |
| Metabolism | CYP3A4 inhibitior | No |
| Excretion | Total clearance | −0.36 |
| Excretion | Renal OCT2 substrate | No |
| Toxicity | AMES toxicity | Yes |
| Toxicity | Max. tolerated dose (human) | −0.11 |
| Toxicity | hERG I inhibitor | No |
| Toxicity | hERG II inhibitor | Yes |
| Toxicity | Oral Rat Acute Toxicity (LD50) | 2.16 |
| Toxicity | Oral Rat Chronic Toxicity (LOAEL) | 1.43 |
| Toxicity | Hepatotoxicity | No |
| Toxicity | Skin sensitisation | No |
| Toxicity | *T.Pyriformis toxicity* | 1.17 |
| Toxicity | Minnow toxicity | 1.02 |

### 3.5. *ADMET profile*

The in silico ADMET evaluation of the synthesized piperinol derivative revealed an overall favorable pharmacokinetic and safety profile, suggesting its potential as a lead scaffold for anticancer drug development. The compound demonstrated moderate water solubility (log $S$ = −4.17), which, although indicative of limited aqueous dissolution, is compensated by excellent intestinal absorption (91.28 %) and appreciable Caco-2 permeability (1.31 log Papp), confirming its suitability for oral administration. The skin permeability (log Kp = −3.29) suggests restricted transdermal diffusion, favoring oral over topical delivery routes. The compound was identified as both a P-glycoprotein substrate and a P-gp I inhibitor, a characteristic that may influence intracellular retention and modulate efflux-related resistance mechanisms—a key consideration in tumor pharmacology where P-gp overexpression often reduces the intracellular concentration of chemotherapeutic agents.

Distribution parameters indicate moderate tissue distribution (VDss = −0.11 log L/kg) and a low fraction of unbound drug (Fu = 0.06), implying significant plasma protein binding that could extend systemic circulation and therapeutic exposure. The negligible brain penetration

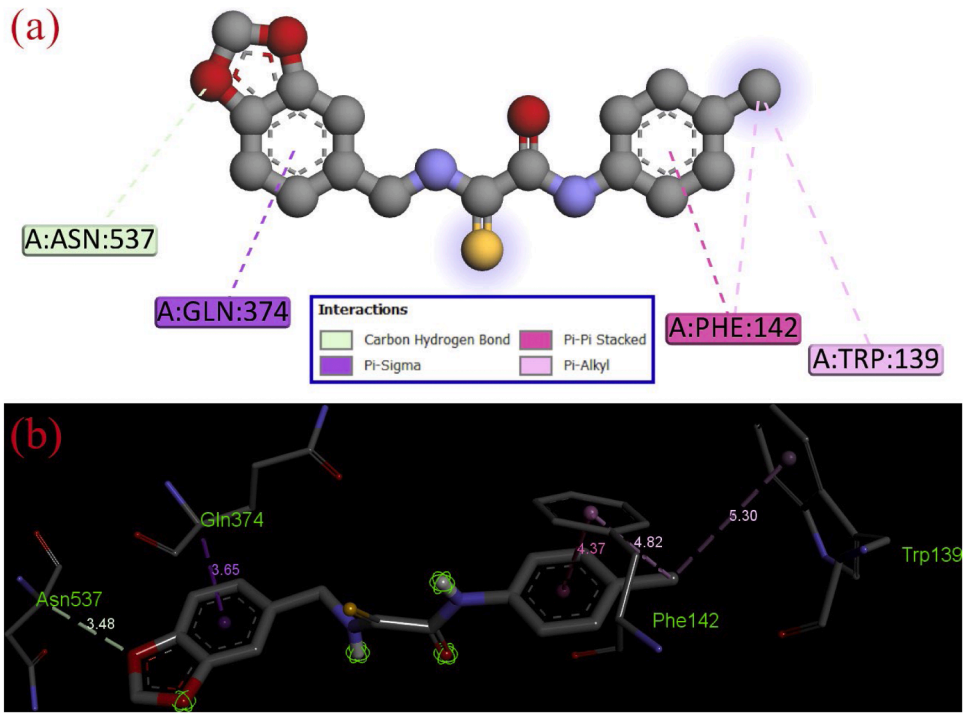


**Fig. 9.** The (a) 2D and (b) 3D interaction diagram reveals the interactions between the **3a** compound and **5F19** protein.

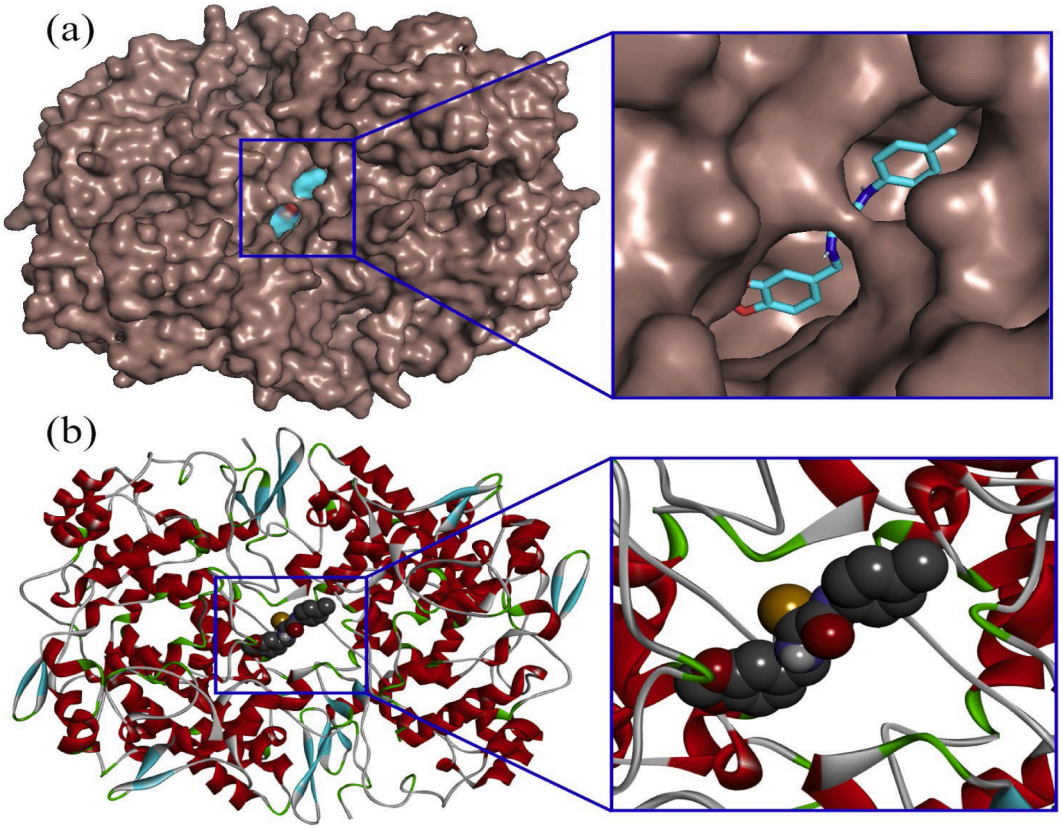


**Fig. 10.** (a) The cartoon (b) surface view of the binding of the **3a** compound with the **5F19** protein.

predicted by BBB permeability (0.19) and CNS permeability (−2.14) values is advantageous for minimizing central nervous system-related adverse effects, particularly desirable for non-CNS anticancer therapy. From a metabolic perspective, the compound is predicted to be a CYP3A4 substrate, reflecting predominant hepatic metabolism, while the absence of inhibitory activity toward CYP1A2, CYP2C9, CYP2D6, and CYP3A4 enzymes suggests a low likelihood of major drug–drug interactions. The observed CYP2C19 inhibition warrants careful

monitoring, as it could influence the metabolism of co-administered substrates of this isoenzyme. Collectively, the predicted metabolism profile denotes satisfactory metabolic stability with a limited risk of poly-CYP inhibition.

The predicted excretion characteristics show a low total clearance rate (−0.36 log mL/min/kg), indicating a moderate elimination half-life and suggesting the potential for sustained systemic exposure. The compound is not a substrate for renal OCT2 transporters, minimizing the risk of renal accumulation or transporter-mediated nephrotoxicity. Toxicological assessment indicated a positive AMES test outcome, implying potential mutagenicity, though such computational predictions often necessitate confirmatory in vitro genotoxicity assays. Importantly, the compound is non-hepatotoxic, non-sensitizing to skin, and devoid of major acute or chronic toxicity liabilities ($LD_{50}$ = 2.16 mol/kg; LOAEL = 1.43 mol/kg), indicating an acceptable safety window for further biological evaluation. Although the compound displayed hERG II inhibition, absence of hERG I blocking activity suggests only a marginal risk of cardiotoxicity, typically observed at higher concentrations. The ADMET profile is provided in the Table 5.

### 3.6. Molecular docking analysis

To explore the biological properties of the synthesized compound and to understand the interaction profile of the ligand with the selected protein (PDB ID: **5F19**) molecular docking analysis was performed (Fig. 9) [52,53]. The novel **3a** molecule exhibits a binding affinity of −7.9 kcal/mol when docked against **5F19** protein. The docking analysis of 3a with the protein 5F19, reveals several key molecular interactions contributing to its binding affinity (Fig. 10). The ligand establishes a carbon hydrogen bond with ASN537 at a distance of 3.48 Å, which helps stabilize the binding *via* interaction with the dioxole ring. A π-sigma interaction is observed between the aromatic ring and GLN374 (3.65 Å), further anchoring the ligand within the binding pocket. On the hydrophobic side, PHE142 forms π-alkyl interactions at distances of 4.37 Å and 4.82 Å, while TRP139 contributes additional π-alkyl interaction at 5.30 Å. These interactions, involving hydrogen bonding and aromatic contacts, collectively contribute to a stable and favorable binding conformation. The ligand's central thioxo-amide linkage facilitates optimal orientation between the two aromatic regions, enhancing its potential as a dual-action therapeutic targeting inflammation and tumorigenesis through soluble epoxide hydrolase inhibition. Further, the molecular docking was performed for the standard drug Doxorubicin and the binding score is found to be −8.7 kcal/mol. The binding pose and its 2D interaction profile is given in the Fig. S7 and S8 respectively.

## 4. Conclusions

This investigation integrates experimental, quantum chemical, and computational approaches to assess the anti-cancer potential of a novel piperonal derivative (**3a**). The crystal structure investigation indicated that the compound crystallized in a monoclinic system with the space group $P2_1/n$. Intermolecular interactions, such as N—H···O and C—H···π, are critical for self-assembly and crystal structure stability. Hirshfeld surface analysis indicated that van der Waals forces, particularly H…H interactions (43.6 %), along with C…H (21.8 %) and O…H (16.8 %), play a significant role in maintaining the crystal's stability The energy gap of the compound is found to be 4.000 eV. The energy gap between frontier molecular orbitals (HOMO and LUMO) indicates that the synthesized molecule is stable and is chemically more reactive. Its band gap energy is equivalent to that of bio-active compounds. The MEP of the compound revealed that the sulfur and oxygen atoms have the highest negative potential and hydrogen atoms of the methoxy group have the highest positive potential, indicating that they are likely to be involved in hydrogen bonding interactions. Molecular docking simulations revealed robust binding affinity of **3a** with protein highlighting their promising anticancer potential.

## CRediT authorship contribution statement

**Darshan D.:** Conceptualization, Formal analysis, Visualization, Writing – original draft. **Santhosh C.:** Methodology, Writing – original draft. **Ravi Singh K.:** Investigation, Methodology, Writing – original draft. **Chethan B. S.:** Software, Visualization, Writing – original draft. **Lohith T. N.:** Resources, Visualization, Writing – original draft. **Sadashiva M. P.:** Writing – review & editing. **Sunil K.:** Project administration, Writing – review & editing. **Hemalatha P.:** Project administration, Supervision, Writing – review & editing.

## Declaration of competing interest

The authors declare that they have no known competing financial interests or personal relationships that could have appeared to influence the work reported in this paper.

## Supplementary materials

Supplementary material associated with this article can be found, in the online version, at doi:10.1016/j.molstruc.2025.144555. CCDC-2475700 contains the supplementary crystallographic data for this paper. These data can be obtained free of charge via https://www.ccdc.cam.ac.uk/structures/, or by e-mailing mailto:data_request@ccdc.cam.ac.uk, or by contacting The Cambridge Crystallographic Data centre, 12 Union Road, Cambridge CB2 1EZ, UK; fax: +44(0)1223–336,033.

## Data availability

Data will be made available on request.

## References

[1] C. Santhosh, K.R. Singh, M.V. Mane, K. Sheela, K. Sharath, M.P. Sadashiva, Base-promoted regioselective synthesis of alkyl (2-tosyl/4-ethylcarbonyl) thiazole-5-carboxylates employing dithioates and active methylene isocyanides, New J. Chem. 49 (11) (2025) 4604–4614.
[2] A. Venkatraman, A.P. Karurkar, S.A.M. Yacoob, S. Muthumanickam, Molecular docking analysis of piperonal and its analogues as promising cancer therapeutics by modulating angiogenesis, J. Drug Deliv. Therapeut. 13 (2023) 1–8.
[3] L. Zhang, C. Li, S. Pang, Dual-aromaticity in nitrogen-rich compounds: from fundamental concepts to the application of high-energy-density materials, Coord. Chem. Rev. 546 (2026) 217081.
[4] W. Xie, Z. Liu, D. Fang, W. Wu, S. Ma, S. Tan, K. Zheng, 3D-QSAR and molecular docking studies of aminopyrimidine derivatives as novel three-targeted Lck/Src/KDR inhibitors, J. Mol. Struct. 1185 (2019) 240–258.
[5] I. Pal Singh, A. Choudhary, Piperine and derivatives: trends in structure–activity relationships, Curr. Top. Med. Chem. 15 (2015) 1722–1734.
[6] R. Singh, C. Santhosh, M. Sridhar, Rationalizing the stability and noncovalent interactions of N-(benzo[d][1,3]dioxol-5-ylmethyl)-2-(methylthio)thiazole-4-carboxamide: insights from X-ray structure and QTAIM analysis, J. Mol. Struct. 1319 (2025) 139407.
[7] A. Maalik, I. Khan, W. Rehman, S. Faiz, A.S. Alanazi, M. Hefnawy, Y. Khan, Discovery of thiourea based acetylcholinesterase inhibitors and antibacterial agents: synthesis, in vitro, structure–activity relationship and in silico study, J. Mol. Struct. 1321 (2025) 140082.
[8] T. Iqbal, S. Khan, R. Hussain, Y. Khan, F. Rahim, A. Hayat, N.S. Awwad, A. G. Alkhathami, A versatile inhibitory approach and molecular mechanism on cancer cells and cholinesterase enzymes: synthesis, DFT, ADMET and molecular docking of thiadiazole and oxadiazole derivatives, J. Mol. Struct. 1322 (2025) 140325.
[9] M. Sapnakumari, B.S. Chethan, T. Jinkle, M.D. Urs, N.S. Lingegowda, N. K. Lokanath, S. Naveen, Multicomponent synthesis, structural and molecular dynamics simulation studies of a novel spirooxindole derivative, Chem. Phys. Impact 8 (2024) 100467.
[10] S.M. Rajesh, D.V. Kumar, V. Shalini, K.B. Harsha, D. Gowda, K.S. Rangappa, Structural analysis and computational studies of cyclopropane derivative as an anti-Alzheimer's agent: investigation of interactions by X-ray crystallography, DFT, molecular docking, and ADMET approaches, J. Mol. Struct. 1430 (2025) 142665.
[11] M. Su, T. Tang, W. Tang, Y. Long, L. Wang, M. Liu, Astragalus improves intestinal barrier function and immunity by acting on intestinal microbiota to treat T2DM: a research review, Front. Immunol. 14 (2023) 1243834.
[12] F. Hassan, C. Liu, M. Mehboob, R.M. Bilal, M.A. Arain, F. Siddique, F. Chen, et al., Potential of dietary hemp and cannabinoids to modulate immune response to enhance health and performance in animals: opportunities and challenges, Front. Immunol. 14 (2023) 1285052.

[13] S. Neetha, C. Santhosh, T. Lohith, K. Sharath, M. Sridhar, M. Sadashiva, Structural elucidation, Hirshfeld surface, DFT, molecular docking and molecular dynamics studies of a novel thiazole derivative as anti-cancer drug, J. Mol. Struct. 1324 (2025) 140793.
[14] V. Karthik, R. Singh, T.N. Lohith, M.B. Leoma, M.A. Sridhar, M.P. Sadashiva, In silico studies of thiazole derivative towards its potential use against SARS-CoV-2: an intuition from an experimental and computational approach, J. Mol. Struct. 1322 (2025) 140475.
[15] Y. Khan, S. Khan, W. Rehman, R. Hussain, A. Maalik, F. Ali, M.U. Khan, A. Sattar, M.A. Assiri, Hybrid molecules of thiadiazole-based benzothioate and benzenesulfonothioate: synthesis, structural analysis, and evaluation as potential inhibitors of thymidine phosphorylase and β-glucuronidase through in vitro and in silico approaches, J. Mol. Struct. 1294 (2023) 136439.
[16] V. Karthik, R. Singh, M.B. Leoma, M. Sridhar, Structure elucidation and computational studies of the thiazole derivative against SARS-CoV-2 virus: insights from XRD, DFT, molecular docking, and molecular dynamics simulation, J. Mol. Struct. 1322 (2025) 140550.
[17] S. Kumar, K. Divya, M. Sridhar, M. Mahendra, A new thiadiazole–triazine derivative: structural investigation, DFT studies, ADME-T analysis and SARS-CoV-2 activity by docking simulation, J. Mol. Struct. 1317 (2024) 139133.
[18] F. Xue, H.D. Preetham, R. Verma, T.N. Lohith, S. Raju, M.S. Ali, V.H. Kameshwar, Structure–property relationship of two gamma-lactam derivatives: hirshfeld surface analysis, DFT, and molecular dynamics simulations, Chem. Phys. Lett. 857 (2024) 141725.
[19] J. Wang, J. Luo, D. Rotili, A. Mai, C. Steegborn, S. Xu, Z.G. Jin, SIRT6 protects against lipopolysaccharide-induced inflammation in human pulmonary lung microvascular endothelial cells, Inflammation 47 (1) (2024) 323–332.
[20] J. Akash, C. Dushyant, C. Jasmine, Piperonal: the journey so far, Mini. Rev. Med. Chem. 20 (2020) 1846–1856.
[21] J. Aukunuru, K. Eedula, V. Pasham, V. Katla, S.K. Reddy, Synthesis of novel piperonal derivatives and evaluation of their anticonvulsant activity using a nanoparticular formulation, Int. J. Pharmaceut. Sci. Nanotechnol. 2 (2009) 435–442.
[22] Q. Dai, Z. Yuan, Q. Sun, Z. Ao, B. He, Y. Jiang, Discovery of novel nucleoside derivatives as selective lysine acetyltransferase p300 inhibitors for cancer therapy, Bioorg. Med. Chem. Lett. 104 (2024) 129742.
[23] M.J. Lucido, B.J. Orlando, A.J. Vecchio, M.G. Malkowski, Crystal structure of aspirin-acetylated human cyclooxygenase-2: insight into the formation of products with reversed stereochemistry, Biochemistry 55 (2016) 1226–1238.
[24] G.M. Sheldrick, Crystal structure refinement with SHELXL, Acta Crystallogr. Section C: Struct. Chem. 71 (2015) 3–8.
[25] K. Harata, Y. Abe, M. Muraki, Crystallographic evaluation of internal motion of human α-lactalbumin refined by full-matrix least-squares method, J. Mol. Biol. 287 (1999) 347–358.
[26] A.L. Spek, Single-crystal structure validation with the program PLATON, J. Appl. Crystallogr. 36 (2003) 7–13.
[27] C.F. Macrae, I. Sovago, S.J. Cottrell, P.T. Galek, P. McCabe, E. Pidcock, P.A. Wood, Mercury 4.0: from visualization to analysis, design and prediction, J. Appl. Crystallogr. 53 (2020) 226–235.
[28] M.A. Spackman, D. Jayatilaka, Hirshfeld surface analysis, Cryst. Eng. Comm. 11 (2009) 19–32.
[29] A. Bhattacharjee, S. Hegde, A.M. Kurumbala, V. Kumar, N. Honnappa, M.S. Ali, M. M. Reddy, Structural elucidation, Hirshfeld surface analysis, DFT, and molecular docking studies of puckered compound: (6aS,12aR)-9-bromo-7,7-dimethyl-6a,7,12,12a-tetrahydro-6H,13H-thiochromeno[3′,4′:5,6]thiopyrano[4,3-b] quinoline, J. Mol. Struct. 1338 (2025) 142135.
[30] D. Jayatilaka, S.K. Wolff, D.J. Grimwood, J.J. McKinnon, M.A. Spackman, CrystalExplorer: a tool for displaying Hirshfeld surfaces and visualising intermolecular interactions in molecular crystals, Acta Crystallogr. Section A 62 (2006) s90, s90.
[31] M.K. Usha, T.N. Lohith, M. Manjula, S. Shetty, B. Kalluraya, D. Revannasiddaiah, M.A. Sridhar, Synthesis, crystal structure, Hirshfeld surface analysis, energy frameworks, and DFT calculations of (2E)-3-(dimethylamino)-1-[5-methyl-1-(4-nitrophenyl)-1H-1,2,3-triazol-4-yl]prop-2-en-1-one, Molec. Cryst. Liquid Crystals 768 (2024) 11–26.
[32] M.P. Andersson, P. Uvdal, New scale factors for harmonic vibrational frequencies using the B3LYP density functional method with the triple-ζ basis set 6-311+G(d, p), J. Phys. Chem. A 109 (2005) 2937–2941.
[33] T.N. Lohith, K. Ravi Singh, M. Feizi-Dehnayebi, C. Santhosh, S. Kishorkumar, M. A. Sridhar, M.P. Sadashiva, Quantitative investigation of the nature of non-covalent interactions in 2-((benzo[d][1,3]dioxol-5-ylmethyl)amino)-N-phenyl-2-thioxoacetamide: insights from crystallographic, DFT analysis, molecular docking, and molecular dynamics simulation, Mol. Phys. (2024) e2444467.
[34] K. Nirusha, H.S. Nagendra Prasad, T.N. Lohith, P. Saravanan, L. Mallesha, A. P. Anand, Exploration of piperazine–citral sulfonyl derivatives: antibacterial and in silico studies against methicillin-resistant *Staphylococcus aureus*, Arch. Microbiol. 207 (2025) 56.
[35] Z. Yan, B. Yu, X. Lan, X. Cui, D. Zhao, L. Qiu, H. Wang, et al., Synthesis, bioactivity evaluation and theoretical study of nicotinamide derivatives containing diphenyl ether fragments as potential succinate dehydrogenase inhibitors, J. Mol. Struct. 1308 (2024) 138331.
[36] Y. Khan, H. Sarfraz, W. Rehman, M. Khan, L. Rasheed, K.U. Rahman, Innovative horizons in drug design: exploring the synthesis and medicinal properties of heterocyclic Schiff bases — A review, Mini-Rev. Medic. Chem. 25 (10) (2025) 727–744.
[37] M.J. Frisch, F.R. Clemente, G.W. Trucks, H.B. Schlegel, G.E. Scuseria, M.A. Robb, et al., Gaussian 09, Revision A.01, Gaussian Inc., Wallingford CT, 2009.
[38] R. Dennington, T.A. Keith, J.M. Millam, GaussView, Version 6.0.16, Semichem Inc, Shawnee Mission KS, 2016.
[39] S. Kumar, K. Divya, M. Sridhar, M. Mahendra, A new thiadiazole–triazine derivative: structural investigation, DFT studies, ADME-T analysis and SARS-CoV-2 activity by docking simulation, J. Mol. Struct. 1317 (2024) 139133.
[40] V. Shalini, A.N. Priyadarshini, B. Harsha Kachigere, D.C. Vinay Kumar, B. S. Chethan, M.S. Sudhanva, S.R. Kanchugarakoppal, Novel quinoline-4-carboxamide derivatives potentiate apoptosis by targeting PDK1 to overcome chemo-resistance in colorectal cancer: theoretical and experimental results, Heliyon. 10 (2024) e2959.
[41] Dassault Systèmes Biovia, Discovery Studio Modeling Environment, Release 2017, Dassault Systèmes, San Diego, 2017.
[42] A. Daina, O. Michielin, V. Zoete, SwissADME: a free web tool to evaluate pharmacokinetics, drug-likeness and medicinal chemistry friendliness of small molecules, Sci. Rep. 7 (1) (2017) 42717.
[43] D.E.V. Pires, T.L. Blundell, D.B. Ascher, pkCSM: predicting small-molecule pharmacokinetic and toxicity properties using graph-based signatures, J. Med. Chem. 58 (9) (2015) 4066–4072.
[44] P. Divya, V.S. Jeba Reeda, P. Rajkumar, A. Amala Jeya Ranchani, R. Shahidha, M. Shahid, N. Siddiqui, S. Javed, Structural insights and ADMET analysis of CAFI: hydrogen bonding, molecular docking, and drug-likeness in renal function enhancers, BMC. Chem. 19 (1) (2025) 36.
[45] R. Huey, G.M. Morris, S. Forli, Using AutoDock 4 and AutoDock Vina with AutoDockTools: A tutorial, Scripps Research Institute, Molecular Graphics Laboratory, North Torrey Pines Road, La Jolla, CA 92037, USA, 2012, 10550.
[46] A.R. Kumar, S. Selvaraj, A.S. Vickram, J. Jenifer, R. Karthik Raja, Experimental and theoretical investigations on antiproliferative compound nootkatone's vibrational characteristics, solvent effects of electronic properties, topological insights, Hirshfeld surface, donor–acceptor insights, ADME, and molecular docking against SMAD proteins, J. Mol. Struct. (2025) 143156, 2025.
[47] T.N. Lohith, K. Sindogi, Unravelling the synthesis, crystal structure, DFT, pharmacophore, and in silico studies of a chalcone derivative: an experimental and theoretical approach, Struct. Chem. (2025) 1–19.
[48] T.N. Lohith, S. Neetha, V.H. Kameshwar, K.S.S. Kumar, M.S. Ali, H.A. Al-Lohedan, S.K. Verma, Structural analysis and computational studies of pyrazole derivative: investigation of interactions by X-ray crystallography, DFT, molecular docking, and molecular dynamics simulation, J. Mol. Struct. 1430 (2025) 143497.
[49] P.S. Pradeep Kumar, K. Sunil, B.S. Chethan, N.K. Lokanath, N. Madan, A.M. Sajith, Synthesis, characterisation, biological and theoretical studies of novel pyridine derivatives, Mol. Phys. 120 (2022) e2093283.
[50] R. Manjula, C. Pavithra, A. Ram Kumar, K. Durgadevi, B. Balraj, S. Selvaraj, A comprehensive investigation into the spectroscopic properties, solvent effects on electronic properties, structural characteristics, topological insights, reactive sites, and molecular docking of racecadotril: a potential antiviral and antiproliferative agent, J. Indian Chem. Society 102 (5) (2025) 101702.
[51] R. Manjula, C. Pavithra, A. Ram Kumar, K. Durgadevi, B. Balraj, S. Selvaraj, Exploring structural and spectroscopic aspects, solvent effect (polar and non-polar) on electronic properties, topological insights, ADME and molecular docking study of thiocolchicoside: a promising candidate for antiviral and antitumor pharmacotherapy, Spectrochim. Acta Part A: Molec. Biomol. Spectros. 331 (2025) 125807.
[52] M. Nagaraju, C.S. Karthik, M.K. Hema, B.S. Chethan, R.J. Ramalingam, M. Karnan, N.K. Lokanath, Perusal on the role of DMF solvent and hydrogen bonding in the formation of 1D polymeric chains in mixed ligand Ni(II) complex as an anticancer agent: a computational approach, J. Biomolec. Struct. Dynamics 43 (2025) 1259–1277.
[53] N. Hegde, S. JS, B.S. Chethan, M.B. Leoma, N.K. Lokanath, Structural, computational and in silico studies of 4-bromo-3-fluorobenzonitrile as anti-alzheimer and anti-parkinson agents, J. Biomolec. Struct. Dynam. 42 (2024) 4619–4643.